Oxidation and burner rig corrosion of liquid phase sintered SiC

D. Baxter [a,*], A. Bellosi [b], F. Monteverde [b]

[a] European Commission, JRC-IAM, Petten, The Netherlands
[b] CNR-IRTEC, Faenza, Italy

Abstract

Liquid phase sintering permits lower temperatures to be used to produce SiC with a consequent saving in terms of cost, while maintaining mechanical properties. For application at elevated temperatures, corrosion resistance must also be maintained. Oxidation in air at 1000 and 1300°C of a SiC sintered with additions of $Al_2O_3 + Y_2O_3$ resulted in protective oxidation kinetics with rates approximately an order of magnitude greater than generally available low-additive SiC. The contaminants present in combustion atmospheres, particularly S and Na, have a marked influence on the rate of material degradation depending on the partial pressure of SO_3 and thus the sulphur content of the fuel. Burner rig tests at 1000°C resulted in high rates of attack due to the formation of a low viscosity Na-silicate surface layer in a low sulphur fuel combustion gas (Jet A1 kerosene). With a low-sulphur fuel (1% S marine diesel) the high SO_3 partial pressure resulted in a low Na_2O activity and limited acid (SiO_2) base (Na_2O) reaction. At 1300°C, similar rates of material degradation were observed. Details of the oxidation kinetics and oxidation product morphologies are given. © 2000 Elsevier Science Ltd. All rights reserved.

Keywords: Burner parts; Oxidation; Electron microscopy (SEM); Corrosion; SiC

1. Introduction

The technical ceramic SiC is one of the promising candidate materials for use in high temperature structural components in applications including heat engines, heat exchangers and wear-resistant components. Solid state sintering at temperatures around 2100°C has become a routine process in the densification of SiC. Unfortunately, such a high processing temperature can result in materials with coarse-grain microstructures and strength lower than 400 MPa. Silicon carbide, like most other ceramic materials, are very sensitive to defects such as pores, cracks and large grains, which contribute to relatively low reliability of structural components[1]. Liquid-phase sintering has the potential to become an alternative commercial method of processing owing to its comparatively low operation temperature (1850–2000°C). The microstructure of LPS-SiC usually is very fine grained (grain size ∼1 μm) and improved strength can be obtained.[2–7] Liquid-phase sintering is achieved by the addition of metal oxides to the

SiC powder, the oxides participating in liquid phase formation at the processing temperatures facilitating rapid mass transport and hence, densification. Densification rates as well as grain growth during liquid phase sintering may be controlled through the manipulation and fine tuning of fabrication parameters and the composition of the sintering aids. The properties of the liquid phase sintered materials are directly dependent upon the properties of the grain boundary phases formed from the liquid phase during cooling.

Generally, solid state sintered silicon carbide offers high oxidation resistance up to 1400°C in simple oxidising environments, due to its ability to form and retain a relatively slow growing surface layer of silica.[8–10] However many potential service environments cannot be characterised as ''simply oxidising'' owing to the presence of aggressive gaseous and condensed species, which may accelerate the rates of corrosive attack. Non-oxide ceramics corrode rapidly in very low oxygen partial pressure environments, particularly where sulphur is present, owing to the formation of volatile oxide and/or sulphide reaction products.[11] In combustion environments, for example in tests performed in burner rigs, strong effects of the presence of contaminants (e.g. Na, Cl and S) in the process environment on the corrosion of

---

* Corresponding author. Tel.: +31-224-6-565227; fax: +31-224-563841.

E-mail address: baxter@jrc.nl (D. Baxter).

non-oxide ceramics have been observed.[8,9,11–13] Fuel sulphur content has a particular effect on the rate of the corrosion reaction when Na and Cl are present as contaminants. Low concentrations of sulphur result in low partial pressures of SO_2 and SO_3, which result in high activities of Na, usually in the form of Na_2O, which in turn leads to an increased rate of breakdown of SiO_2 by Na.[13] In general, the rate of corrosion is determined mainly by the transport of reacting species across a silica-rich surface film, but the actual composition of the surface film depends to a large extent on sintering agents added to permit the achievement of fully dense ceramics. In liquid phase sintered (LPS)-SiC, an important role of the grain boundary phases on oxidation or corrosion is therefore expected,[16–19] by analogy with the behaviour generally observed in additive-containing silicon nitride-based materials.[8,12,14]

Moreover the interaction of these non-oxide multi-phase ceramics in hostile environments generates new strength-degrading flaws[8] which will act as the main life-limiting factor of the proper structural integrity and reliability on service. An important challenge from the corrosion standpoint is therefore the identification of the attack sites and the related microstructural modifications which generate critical defects.

In this paper, the corrosion behaviour of a LPS-SiC hot pressed with additions of metal oxides (Al_2O_3 and Y_2O_3) was studied in a salt contaminated combustion environment at 1000 and 1300°C for times up to 50 h. The data were compared with the results obtained from oxidation tests for the same times and temperatures, in order to evaluate the influence of the contaminants on the oxidation/corrosion mechanisms and to ascertain the role of the grain boundary phases in both types of exposure environment. Strength degradation after corrosion/oxidation was also evaluated.

2. Experimental methods

2.1. Test material

Starting from SiC powder (HCST BF-12, Berlin, Germany, 97 wt% β-SiC and 3 wt% α-SiC, specific surface area: 11.6 m^2/g, chemical composition: C = 30.2 wt%, O = 0.9 wt%, Fe = 340 ppm, Al = 210 ppm, Ca = 15 ppm), the following composition was prepared using additive powders: Al_2O_3 (Baikalox CR30, Baikowski Chimie, Annecy, France), Y_2O_3 (HCST grade C, Berlin, Germany):

90 wt% SiC + 6 wt% Al_2O_3 + 4 wt% Y_2O_3
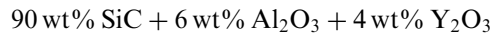
The mixture was hot pressed at 1850°C and 30 MPa. Details of the production processing are given elsewhere.[7] Some selected properties are shown in Table 1.

The crystalline phases in the hot pressed materials found by X-ray diffraction were β-SiC, $3Y_2O_3.5Al_2O_3$ (YAG, estimated to be 7 vol% from a comparison of XRD peak intensities), traces of α-SiC and unreacted alumina. An amorphous Al-silicate (about 4 vol%) is deduced to have formed from the reaction of the additives and impurities with pre-existing silica on SiC surface particles.

Typical microstructural features of the hot pressed materials are shown in Fig 1. Grain sizes ranged from 0.1 to 2 μm. The grain shape was mainly equiaxed. Intergranular phases (bright network in the SEM pictures) are mainly at three- and four-grain pockets: in
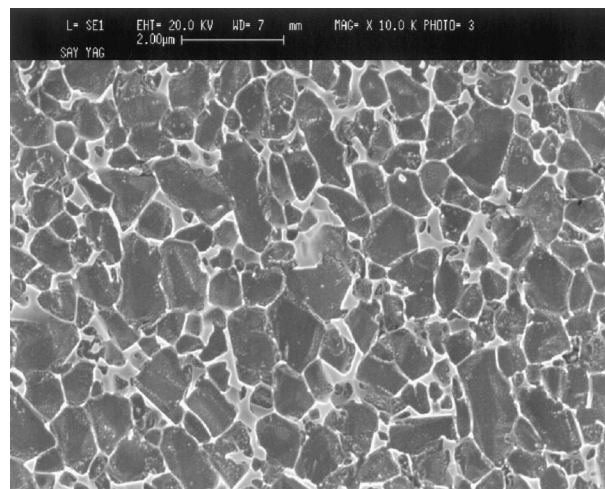

Fig. 1. SEM micrograph of a polished and etched surface of the LP-sintered material.

Table 1
Typical properties of the material studied[a,b]

Density		Mean grain size (μm)	HV1.0 (Gpa)	K_{IC} (MPa$\sqrt{m}$)	σ (MPa)			E (GPa)
(g/cm³)	(%)				RT	1000°C	1300°C	
3.24	98.8	0.5	22.0 ± 0.8	2.97 ± 0.15	656 ± 58	528 ± 53	159 ± 7	386

[a] Vickers microhardness (HV1.0) obtained with a load of 1.0 kg; fracture toughness (K_{IC}) by direct crack measurement (DCM) method (10 kg); Young's modulus (E) by resonance frequency method on samples 28×8×0.8 mm; strength (σ) by 4-point method on 2×2.5×25 mm (inner span 10 mm, outer span 20 mm, crosshead speed: 0.5 mm/min).
[b] Data from Ref. 7, except RT strength, which is for the batch of material used in this study.

these areas the YAG phase was identified by EDX analyses, while amorphous grain boundary phases are located along adjacent SiC grains. Polished and etched surfaces revealed a core/rim structure inside the SiC grains (Fig. 1). EDX analyses confirmed differences in the core to edge compositions: in the core region only Si and C were detected while traces of Al and O were observed in the outer shell.[7] This feature partially agrees with previous observations that report the presence in the outer rim of Al, Y and O.[15]

2.2. Test methodology

The test pieces for corrosion and oxidation tests were machined from as-sintered discs 40 mm diameter and 15 mm thick to the dimensions $2.0 \times 2.5 \times 25$ mm according EN 843-1. The final surface roughness was < 1 μm (R_a).

2.2.1. Burner rig tests

For each test, bars were placed vertically with the bottom 2 mm supported in a rotating (to ensure uniform exposure of all faces), alumina-coated metal table in a low-velocity (0.2 m s^{-1}) burner rig. The tests were carried out at temperatures of 1000 and 1300°C each for a total time of 50 h, divided in eight equal cycles of 6.25 h. After each thermal cycle the bars were cooled freely in laboratory air and weighed. The corrosion environment was produced by burning either a 1 wt% sulphur marine diesel fuel or a 0.01 wt% sulphur kerosene (Jet A1) in air contaminated with artificial ocean water. The ocean water was made to the standard ASTM D1141 (containing the following proportions of salts, by weight; 59% NaCl, 10% Na_2SO_4, 26% $MgCl_2.6H_2O$, 3% $CaCl_2$ and 1.7% KCl). The ratio of air to fuel was 28:1 (by weight) and resulted in a nominal input of 310 or 31 ppm of SO_2, for 1 and 0.01% sulphur fuels, respectively. The total flux of sea salt injected into the burner rig was 13 mg cm^{-2} h^{-1}, which is equivalent to 4 mg cm^{-2} h^{-1} of Na. Calculations of the combustion gas compositions using the Solgasmix computer program[20] (assuming thermodynamic equilibrium) showed that no condensed phases should be produced in either of the two combustion gases at both temperatures of test. The simultaneous exposure of pure alumina (considered

inert) test pieces confirmed that no condensation occurred during the actual tests. The partial pressures of the main combustion products are listed in Table 2.

2.3. Oxidation tests

A laboratory muffle furnace with essentially static laboratory air was used to carry out oxidation tests at 1000 and 1300°C for repeated exposures of 10 h to a total time of 50 h. The test bars, supported horizontally on platinum rings in the furnace, were weighed at room temperature after cooling freely in laboratory air after each 10-h exposure.

2.4. Mechanical tests

Flexural strength tests were carried out in accordance with EN843-1 on material in both the as-received condition and after oxidation or burner rig testing. A four-point jig was used with outer span of 20 mm and inner span of 10 mm. The rate of loading was 0.5 mm/min. The calculation of strength used the original test piece dimensions taken before any oxidation or burner rig corrosion treatments.

2.5. Microstructural analysis

The morphology and structure of the corroded surfaces were analysed by XRD and SEM-EDX. In addition, polished cross sections of the test pieces were examined by SEM-EDX to evaluate the thickness and composition of the oxidation products, the morphology of the reaction interface and the microstructure of the sub-scale material.

3. Results

3.1. Burner rig corrosion

The weight changes for all test pieces exposed to the 0.01% S and 1% S fuel combustion gases at 1000 and 1300°C are shown in Fig. 2. Only a small amount of scatter in the data for each test condition was observed, caused in most cases by the loss of varying amounts of

Table 2
Partial pressures (Pa) of the main species in the combustion gases[a]

	Fuel (wt% S)	pSO$_2$	pSO$_3$	pNaOH	pNa$_2$O	pNa$_2$SO$_4$
1000°C	0.01	1.6×10^{-1}	1.1×10^{-2}	1.4×10^{-1}	9.9×10^{-10}	6.6×10^{-2}
1300°C	0.01	2.8×10^{-1}	3.2×10^{-3}	7.9×10^{-1}	2.1×10^{-8}	1.1×10^{-4}
1000°C	1.0	2.8×10^{1}	1.8×10^{0}	1.1×10^{-2}	1.1×10^{-11}	6.6×10^{-2}
1300°C	1.0	3.1×10	3.6×10^{-1}	7.7×10^{-1}	2.0×10^{-8}	1.1×10^{-2}

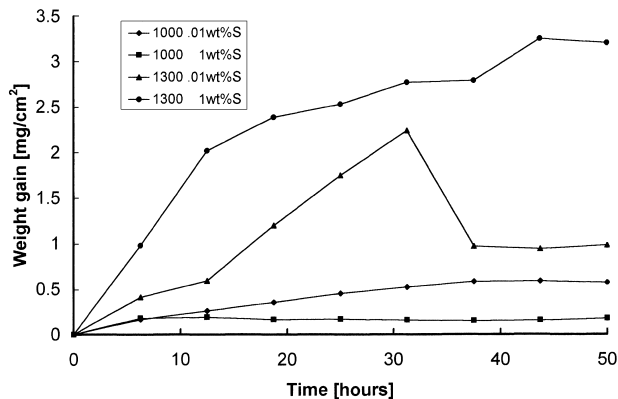[a] Total pressure: 10^5 Pa.

Fig. 2. Summary of weight changes after exposure to the 0.01% S and 1% S fuel combustion gases at 1000 and 1300°C.

low-viscosity glassy corrosion products during the test and upon removal of the test pieces from the holders for periodic weighing. Nevertheless, definite trends in weight change behaviour emerged (Fig. 2). First, the amount of corrosion in the 0.01% S fuel combustion gas at 1000°C was greater than in the 1% S combustion gas, and the respective corrosion rates followed different relationships. In the 0.01% S gas the rate of weight gain was approximately parabolic, whereas in the 1% S gas, after an initial period of very rapid weight gain, no significant further gain of weight was observed. Second, the amount of corrosion in the first 30 h of exposure at 1300°C was essentially independent of combustion gas composition, although in the 0.01% S gas the rate of weight gain was linear and in the 1% S gas the rate was approximately parabolic. Owing to the limitations of weight change data in accurately describing corrosion behaviour, due mainly to the occasional lost of molten and/or friable corrosion products, the main analysis of the test material is based on microstructural observations.

3.1.1. 0.01% S fuel

Analyses of the SiC surfaces by XRD revealed the major crystalline phase present to be crystobalite after testing at 1000°C (Table 3). As seen in SEM micrographs [Fig. 3(a) and (b)], the surfaces were completely covered by a 5–40 µm-thick layer of glassy silicate which cracked on cooling. In the silicate were agglomerations of large (up to 50 µm) bubbles resulting from localised escape of gas generated by the oxidation process, as well as a few small crystals of yttrium disilicate. The glassy silicate contained, in addition to Si and Al, Na as well as traces of K and Fe. Examination in cross section revealed a two-layer surface scale. The outer layer comprised the Na,Al-silicate glass, while a uniformly thick crystalline silica (α-cristobalite according to XRD) constituted the inner layer [Fig. 3(c)–(e)]. Fig. 3(e) shows a zone of preferential grain boundary attack where the silica crystals are located mainly at the reaction interface, following the irregular profile of the advancing corrosion front into the bulk ceramic. Numerous gas bubbles were present immediately beneath the crystobalite layer [Fig. 3(c) and 4], in some cases the bubbles being associated with localised zones of enhanced internal oxidation of the ceramic. The localised internal oxidation of the ceramic resulted in the formation of additional silicate glass as well as crystobalite. The X-ray maps in Fig. 4 show in particular the distribution of Na in the internal oxidation "pit". Cracks predominated in the crystobalite layer mainly perpendicular to the surface of the ceramic substrate. Crack propagation into neither the glassy phase nor the ceramic was observed.

After exposure at 1300°C (Fig. 2), following the 30-h period of linear weight gain (rate constant 1.2×10^{-3} mg/cm^2 min), weight loss of all test pieces was observed in the remaining time of test. A general view of the corroded surfaces [Fig. 5(a)] shows two main features: (i) gas bubbles and holes with adjacent Na- and Al-rich zones in addition to oriented $Y_2O_3.SiO_2$ platelike crystals, and (ii) areas of cracked glassy phase, containing the same elements found adjacent to the bubbles, but with slightly lower Al and Na contents. The fractured and polished cross sections [Fig. 5(b) and (c)] reveal complex, graded microstructures. In the outer part of the corrosion product, a mainly glassy layer (10–60 µm thick) contains the yttrium silicate crystals and bubbles. Under this, a layer (up to 50 µm thick) containing partially reacted SiC particles in a glassy phase was present. The glassy phase extended into the bulk of the unreacted ceramic to form pits. Inside the glassy areas, pores were

Table 3
Crystalline phases on the corroded surfaces and thickness (τ) of the reaction layer after exposure for 50 h at 1000 and 1300°C under burner rig corrosion and after oxidation in air

Temperature (°C)	Atmosphere	β-SiC	YAG	α-Crystobalite	$Y_2Si_2O_7$ Keiviite	τ (µm)
1000	1 wt% S	Y[a]	Y	Y	Traces	<2
1000	0.01 wt% S	Y	Y	Y	N	5–40
1300	1 wt% S	Y	N	Y	N	50–100
1300	0.01 wt% S	Y	traces	Y	Y↑[b]	10–15
1000	Air	Y	Y	Y	Traces	~1
1300	Air	Y	N	Y	Y↑↑	10–20

[a] Y: detected, N: not detected.
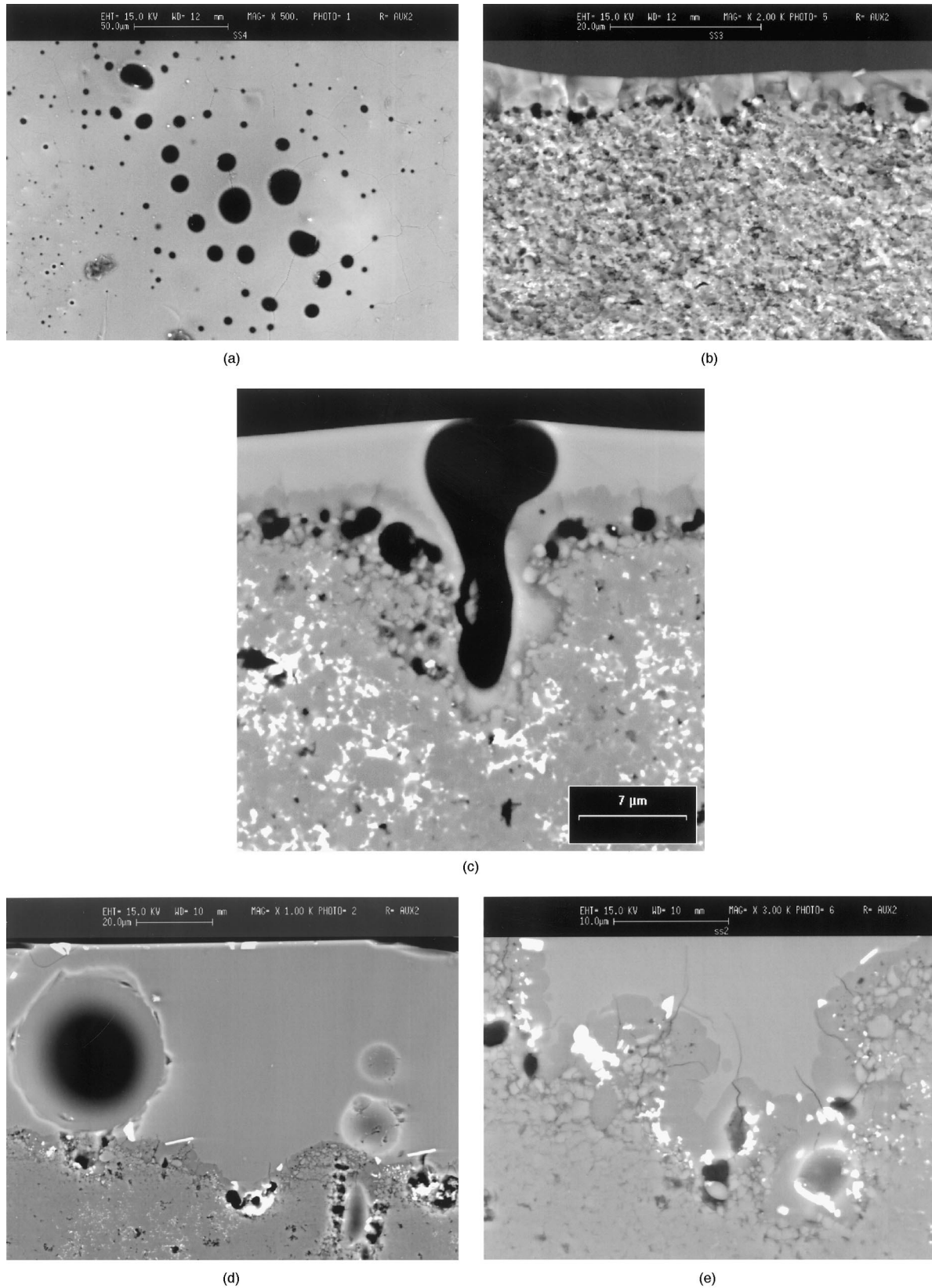[b] ↑ indicates a preferred orientation.

Fig. 3. SEM micrographs taken after exposure for 50 h to the 0.01% S combustion gas at 1000°C: (a) the outer surface showing agglomerations of burst gas bubbles; (b) a fracture section through scale and ceramic; (c) transverse cross section showing a gas bubble extending from the outer surface of the glassy layer into a pit in the base ceramic; (d) and (e) transverse sections showing the uniform Na-silicate glass outer layer and the tightly packed crystobalite layer following the contours of the oxidised ceramic surface.

found. The morphology of the oxidised ceramic surface is shown in Fig. 5(c). As after exposure at 1000°C, gas bubbles were associated with zones where accelerated oxidation had taken place, in some cases agglomerations of yttrium silicate particles were also present around the internal attack zones. The depth of depletion of yttrium
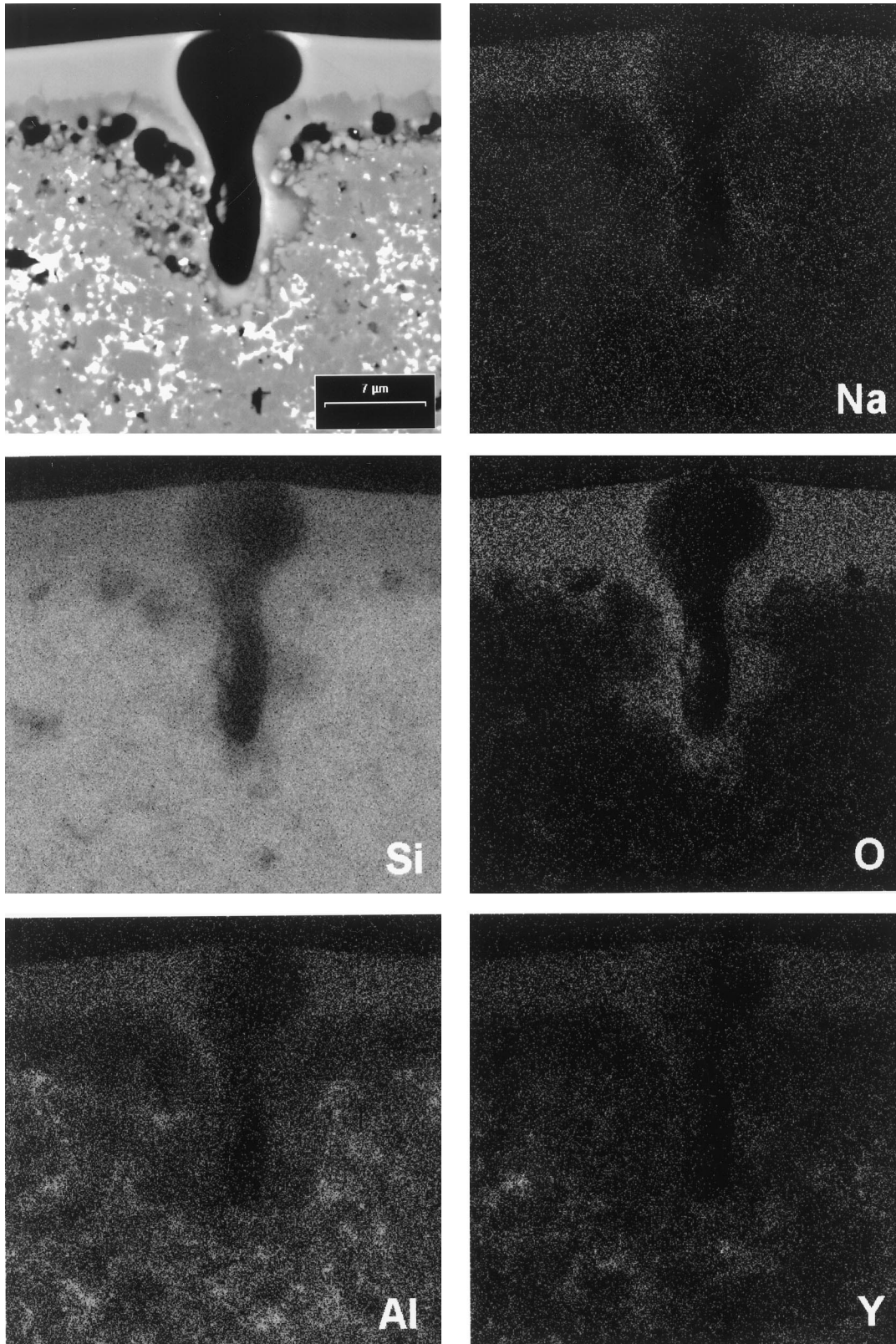
Fig. 4. X-ray maps showing the distribution of elements in the area of the pit shown in Fig. 3(c).
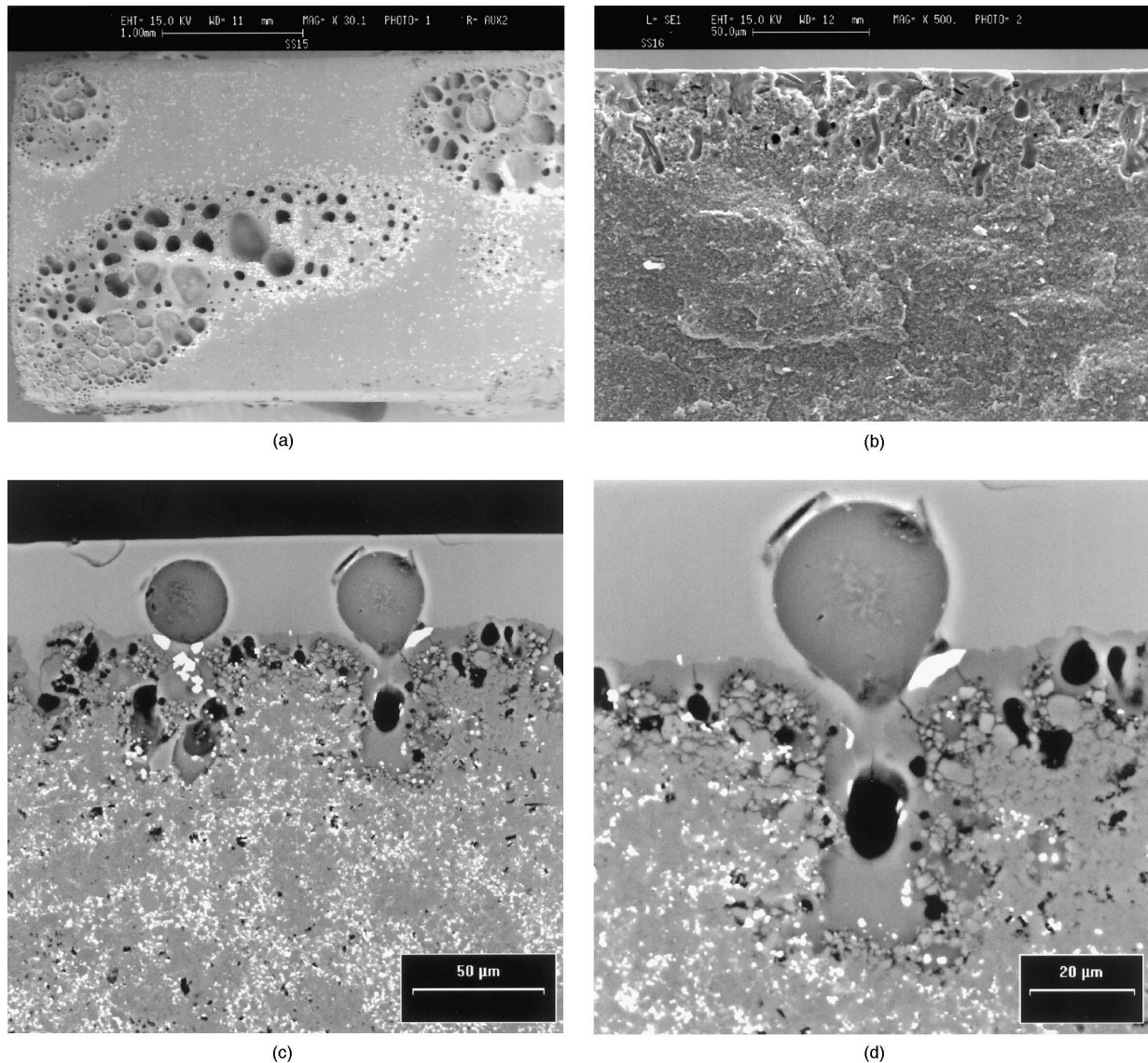
Fig. 5. A general view of the corroded surfaces after 50 h in a 0.01% S fuel combustion gas at 1300°C: (a) gas bubbles and holes with adjacent oriented $Y_2O_3 \cdot SiO_2$ crystals (white) on the outer surface; (b) fracture section showing pitted sub-surface of the ceramic; (c) polished cross section showing the distribution of bubbles and interfacial pores; (d) higher magnification of (c) showing intergranular oxidation and crystobalite formation in the vicinity of a surface pit.

ranged from almost nothing to 100 μm, with areas of deep depletion usually being accompanied by closely spaced zones of internal oxidation [Fig. 5(c)]. Cracking was again restricted to the crystobalite layer, but in regions where the intergranular material had been depleted, cracks appeared to extend intergranularly into the base ceramic [Fig. 5(d)]. The blunt, wedge-shaped "pit" shown in Fig. 5(d) is typical of the morphology of the internal attack of the material at 1300°C.

3.1.2. 1% S fuel

At 1000°C, an initial sharp increase in weight (about 0.2 mg/cm²) in the first 6.25-h exposure was followed by a nearly constant regime with some slight variation for each test piece [Fig. 2]. The surface scale was continuous

and very thin (< 2 μm), with isolated yttrium silicate crystals. The thinness of the scale left clear evidence of polishing marks produced during the test specimen preparation [Fig 6(a) and (b)]. Discrete areas (some exceeding 100 μm diameter) of glassy phase were found: the EDX analysis showed the presence of traces of K, Ca and Fe in addition to Si and small amounts of Al and Na. In cross section, isolated areas of internal oxidation of the ceramic up to 5 μm deep were found [Fig. 6(c)]. No Y depletion zone was apparent.

At 1300°C [Fig. 2], the weight increased up to a maximum of about 3.5 mg/cm² in essentially two linear stages: up to 12 hours (rate constant of 2.7×10^{-3} mg/(cm² min) and subsequently up to 50 hours (rate constant of 5.8×10^{-4} mg/(cm² min). A combination of the
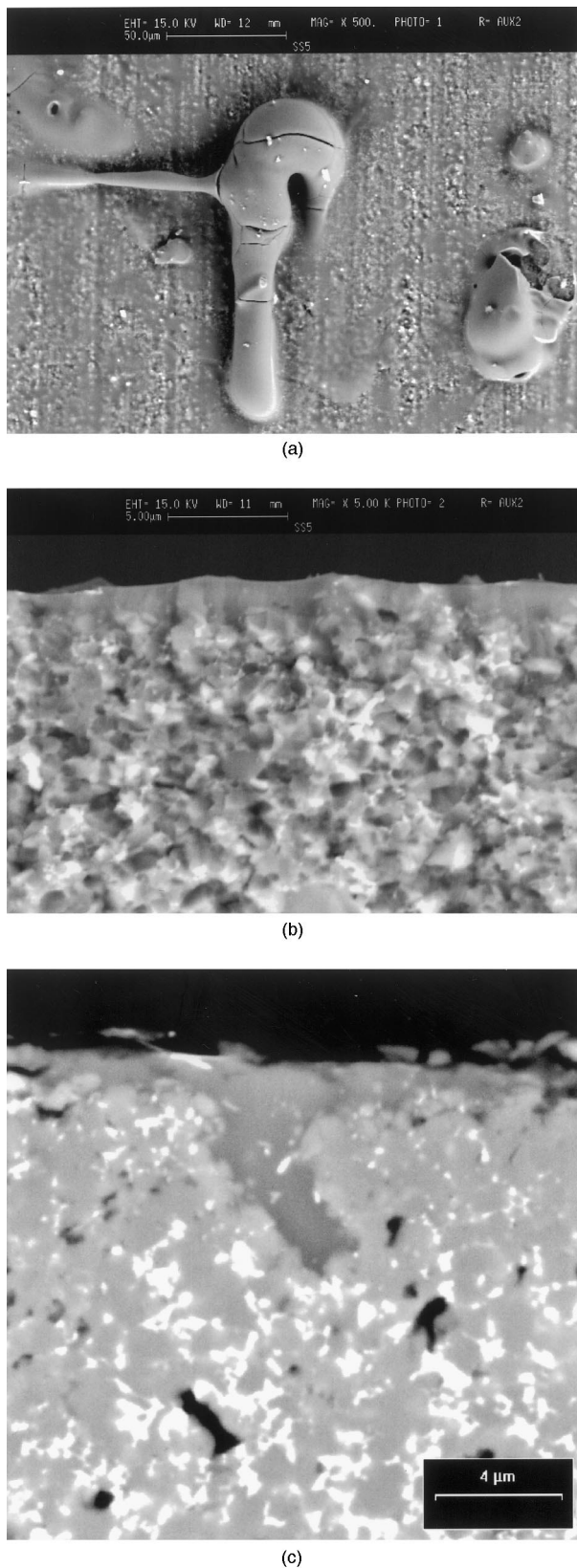
(a)

(b)

(c)

Fig. 6. SEM micrographs taken after exposure for 50 h to the 1% S combustion gas at 1000°C: (a) the outer surface with large blisters on the otherwise thin surface scale; (b) fracture section through an area of very thin scale; (c) polished cross section through a pit filled with oxidation product.

formation of large amounts of a very low viscosity glassy silicate, and surface tension effects resulted in localised bulging of the corrosion products. In these area [Figs. 7(a) and (b)] the glassy phase contained large bubbles (some exceeding 500 μm diameter) and agglomerations of oriented plate-like crystals of Y-silicate. The glass was composed mainly of an Al,Na silicate with traces of K and Ca. The fracture cross section [Fig. 7(c)] showed a double-layer corrosion product morphology. The outer glass corrosion product (up to about 100 μm thick) contained bubbles and Y-silicate crystals. An inner zone (20–50 μm thick) was composed of a glassy phase locally penetrating the SiC ceramic, mainly an grain boundaries. Again the interface between corrosion products and base ceramic was difficult to define on the fracture faces. On polished cross sections, the rough, undulating morphology of the interface between corrosion products and substrate material is clearly evident [Fig. 7(d)]. The depth of depletion of yttrium beneath the ceramic surface ranged from 10 to 50 μm, regardless of the thickness of the surface scale, which varied between 10 and 100 μm. Localised internal attack of the ceramic reached depths of 150 μm. The distributions of elements in a region of internal oxidation are shown in Fig. 8. Cracks were also seen to extend from the crystobalite at the base of the surface scale into films of crystobalite lining the zones of enhanced internal oxidation as in Fig. 3(e). Again, it appeared that crystobalite crystals form exactly at the surface oxide/SiC interface. From their location and morphology, it seems that they are produced by the direct conversion of SiC grains to SiO_2, and/or by the ceramic surface providing nucleation sites for crystobalite precipitated from the glassy melt. Subsequently, however, the crystobalite crystals may break free from the interface (Fig. 9) and "float" towards the outer part of the silicate layer, where they (re)dissolve.

3.2. Oxidation

The weight gains of the test pieces during oxidation in air at 1000 and 1300°C are shown in Fig. 10. A progressively decreasing weight gain suggests some form of diffusion control in the formation of a passivating layer on the surface of the ceramic. The data, however, do not fit a parabolic model for the entire duration of exposure.

XRD analyses on the surface of the oxidized samples revealed, as crystalline oxidation products, yttrium disilicate ($Y_2O_3.2SiO_2$) and α-crystobalite (Table 3). A very thin (~1 μm) mainly glassy layer with very few yttrium disilicates (Fig. 11) formed during 50 h at 1000°C. After 50 h at 1300°C the thickness of the surface oxidation scale ranged from 10 to 20 μm. The upper surface of the oxide scale was covered by highly oriented $Y_2O_3.SiO_2$ plate-like crystals (Fig. 12), most of them aligned in a layered structure inside the glassy layer. Evolution of
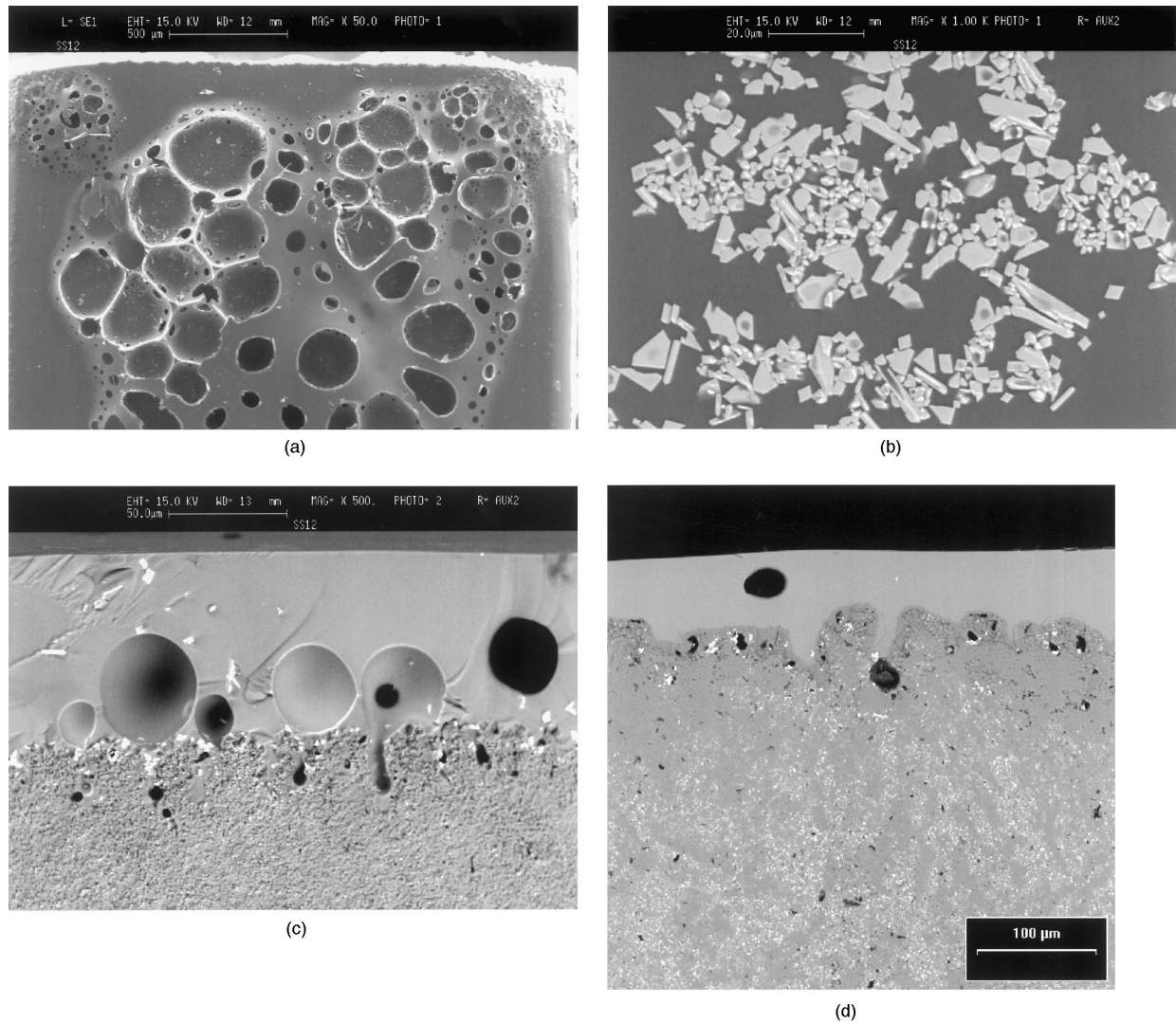
Fig. 7. SEM micrographs taken after exposure for 50 h to the 1% S combustion gas at 1300°C: (a) the outer surface with zone of burst gas bubbles; (b) agglomerations of oriented Y-silicate crystals on the outer surface of the glass; (c) fracture cross section revealing the presence of gas bubbles adjacent to the ceramic surface, sometimes extending into sub-surface pits in the base ceramic; (d) polished cross section showing the undulating morphology of the interface between corrosion products and substrate material.

volatile species (e.g. CO) led to bubbles of several microns in size within the glassy layer. Escape of gas from the outer surface of the scale left behind ruptures (from burst bubbles). The oxidation products appeared adherent to the base ceramic with a pore free interface. No evidence of oxidation induced changes in the base ceramic were observed. Indeed, polished and plasma etched cross sections [Fig. 13(a) and (b)] revealed, along the sharp interface between the surface scale and the ceramic, a continuous row of α-crystobalite grains. The EDX analyses showed the presence of Y, Si and O in the highly textured plate-like crystals deduced to be the yttrium-disilicates, while in the glassy oxidation product, Y, Si and Al as well as traces of Na, K, Ca and Fe were found. Yttrium and aluminium are presumed to have been transported towards the reaction interface from the base ceramic; the trace elements were present

as impurities in the SiC raw powder and were concentrated at grain boundaries after sintering. During oxidation, most of the Y ions diffuse and combine with silica forming the plate-like crystals, whereas the other elements remain dissolved in the glassy matrix.

3.3. Strength degradation

From the values shown in Table 4, the room temperature flexural strength was found to slightly increase after exposure at 1000°C in 1% S fuel, probably due to the thin surface film smoothing over previously existing (sub-)surface flaws. There was a negligible change in strength after oxidation in air, however, this was accompanied by an increase in the scatter of data. A strength reduction ranging from 29 to 35% occurred after exposure in the burner rig in 0.01% S fuel com-
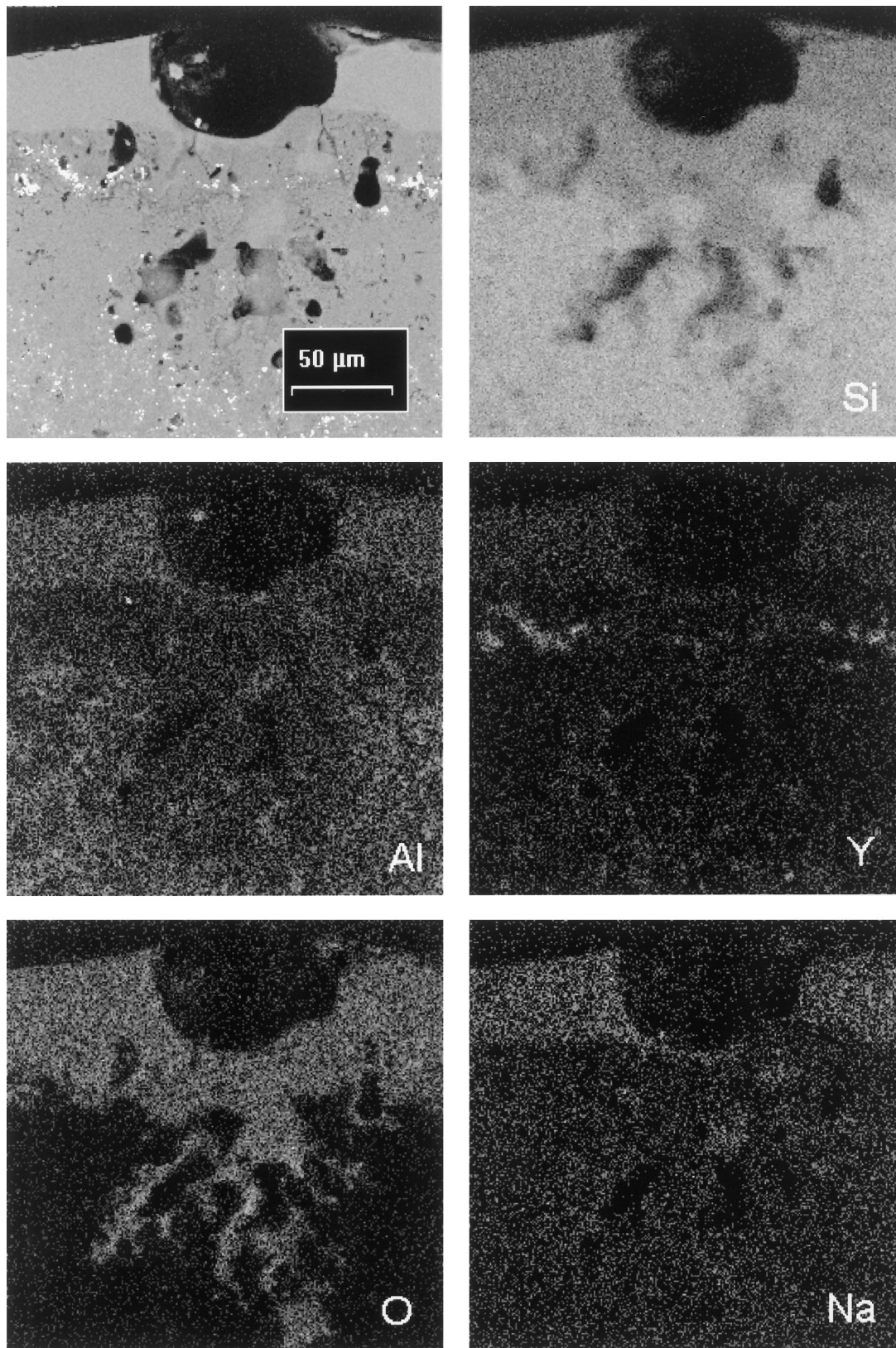
Fig. 8. X-ray maps showing the distribution of elements in an area around a pit after 50 h exposure at 1300°C to the 1% S fuel combustion gas.
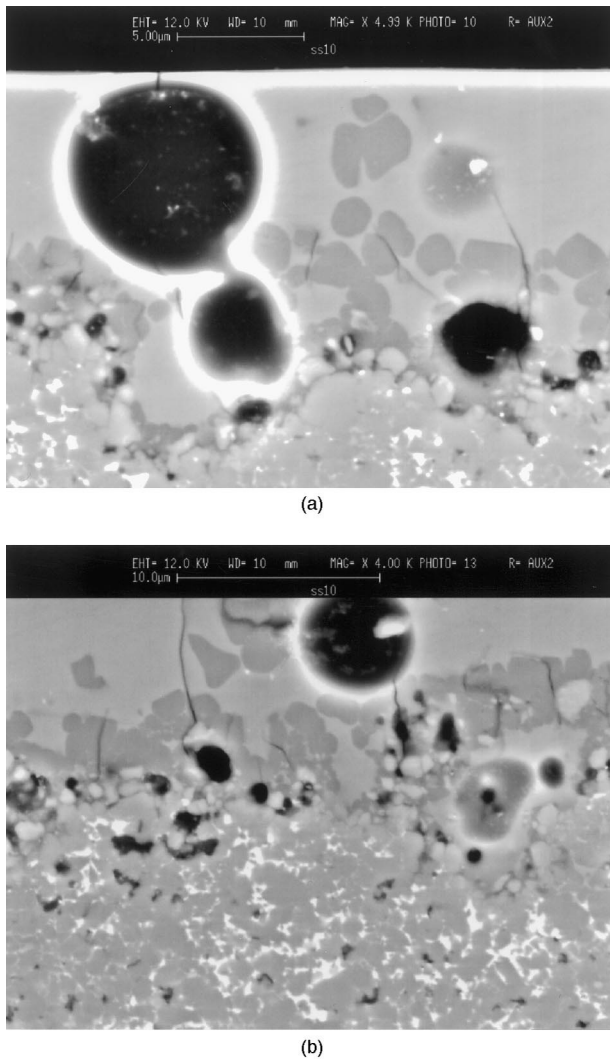
(a)

(b)

Fig. 9. SEM micrographs taken after exposure for 50 h to the 1% S combustion gas at 1300°C: (a) and (b) polished cross sections showing the break away of crystobalite crystals away from the ceramic surface.

bustion gases at both 1000 and 1300°C. Examination for defects revealed in some cases intrinsic internal flaws in the bulk material [Fig. 14(a)] and in other cases surface flaws due to the corrosive/oxidizing attack [Fig. 14(b)].

4. Discussion

The degradation of silicon-based ceramics in oxidizing/combustion environments is influenced by a number of processes (oxidation, deposit-induced corrosion, scale/substrate interactions, scale volatilization, etc.), the importance of each depending on the actual conditions of exposure. The critical process and the sequence of events occurring throughout the life of a component are often difficult to establish. LP sintered materials in combustion environments add a number of complexities to the fundamental oxidation processes. These com-

plexities derive from the effects of sintering additives that become involved in the oxidation/corrosion process leading to modification of the oxidation product composition and morphology. The transport of numerous different species from the bulk ceramic to the reaction interface, simultaneous reactions at the interface and inside the growing scale, scale melting and crystallization of the silica-rich surface layer can result from the presence of the sintering additives.

In either air or combustion gases, the main reaction is that of SiC with oxygen to form SiO_2,

$$2SiC\,(s) + 3O_2\,(g) \Rightarrow 2SiO_2\,(s) + 2CO\,(g) \qquad (1)$$
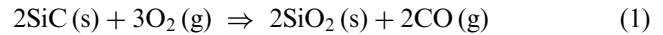
the main component of the surface scale. The presence of additives/impurities from the bulk (due to diffusion and/or grain boundary attack) and the reaction of these species with the growing oxide film on the surface lead to modification of the silica-based scale. Yttrium disilicate crystals are one the main products.

$$2SiO_2 + Y_2O_3 \Rightarrow Y_2Si_2O_7 \qquad (2)$$
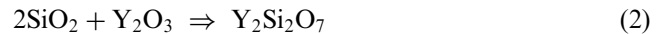
In general, the oxidation product is composed of three main components, a continuous glassy silicate layer (containing additives and contaminants) with plate-like yttrium disilicate crystals mainly located in the vicinity of the outer surface and α-crystobalite at the ceramic surface. The zone of ceramic immediately adjacent to the oxidised surface material is depleted in grain boundary phases and is subject to a localised pitting form of attack. Crystobalite crystals (particularly evident in Figs. 3(d) and (e), 5(c) and (d), 6(c), 9(a) and (b) 13(a) and (b)] nucleate and grow on the surfaces of the SiC grains. Particles of crystalline SiO_2 that become detached from the interfacial layer move freely in the silicate glass redissolving if they approach the outer gas interface [Fig. 9(a) and (b)].

Cracks in the surface scale, perpendicular to the ceramic–oxide interface, are deduced to have been caused during cooling due to thermal expansion mismatch between the α-cristobalite and the glassy silicate or the base ceramic. Once the crystobalite was cracked, repair appeared to be slow whereas cracking of the glass was quickly repaired upon re-exposure at high temperature. The evolution of the oxidation/corrosion behaviour is closely dependent upon the experimental conditions: the presence of contaminants in the atmosphere (most importantly alkali metals such as Na) determines transport phenomena across the surface silica-based surface glassy scale and the tendency for devitrification.

4.1. Oxidation in air

The weight gain curves (Fig. 10) show a clear decelratory mode of scale growth which is the result of the
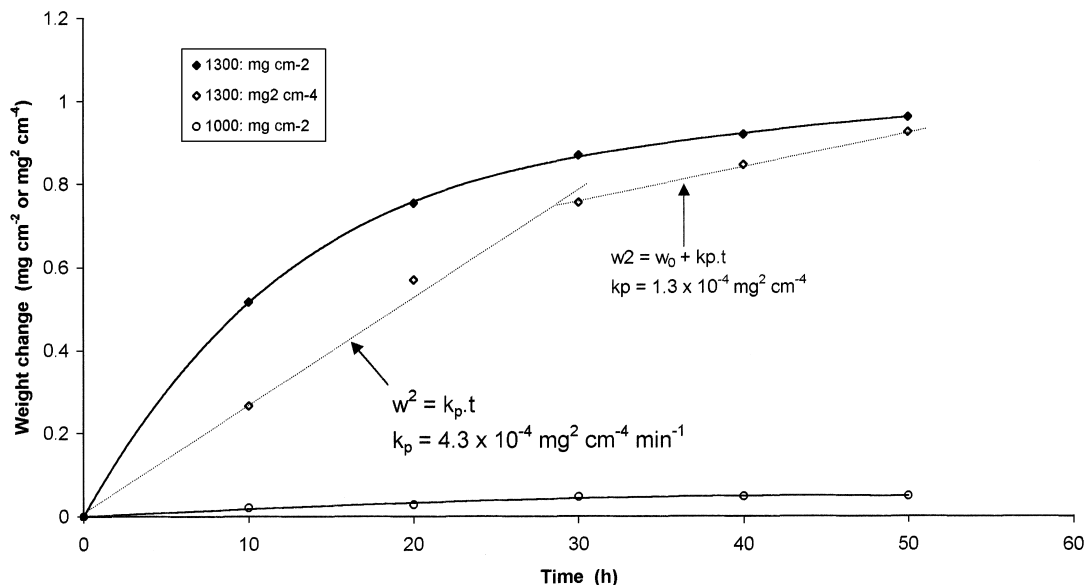
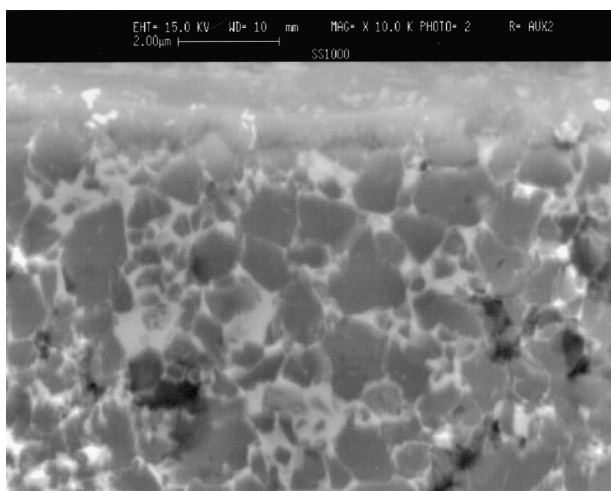Fig. 10. Weight change data for oxidation in air at 1000 and 1300°C.

Fig. 11. SEM micrograph of a cross section through the ceramic oxidised for 50 h at 1000°C: a very thin (~1 μm) mainly glassy layer with very few yttrium disilicates were formed.
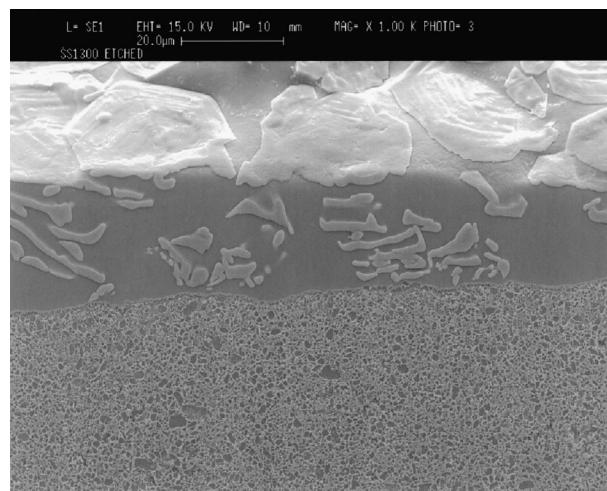

Fig. 12. SEM micrograph of a plasma etched section through ceramic and surface scale showing in particular the "pancake" morphology of the oriented $Y_2O_3.SiO_2$ crystals after oxidation for 50 h at 1300°C. [Note that the micrograph was taken with the unmounted sample tilted to show both the transverse cross section (middle third of picture) as well as the outer surface of the surface scale (top third of the picture).]

formation and growth of a protective silica-rich scale containing both crystalline and amorphous components as well as yttrium disilicates. While oxygen is the only element from the gaseous atmosphere participating in the reaction, numerous elements in the base ceramic including the sintering additives (Y, Al) and impurities (Na, K, Ca, Fe) take part in the scale forming process. In the literature,[8–10,21] the excellent oxidation resistance of pure CVD SiC and solid state sintered SiC has been explained on the basis of the slow diffusion of oxygen through the silica that forms on the surface following reaction (1). In LP sintered SiC the oxidation is predominantly affected by the characteristics of the grain boundary phases, i.e the nature and content of additives

and impurities rather than by the intrinsic oxidation of the silicon carbide to silica.[8,9,16–18] In general, high additive or impurity contents can lead to substantial increases in the oxidation rate which in turn leads not only to differences in published data for materials of the same class, but also to a lack of close agreement of the mechanisms involved.

Both the kinetic data in Fig. 10 and the results of microstructural investigations confirm that diffusion processes are likely to be involved in the rate-controlling oxidation mechanisms. However, several factors, occurring concurrently with the base reaction (1), have

important influences on the overall behaviour. These include the reduction of the viscosity of the glassy scale, due to the presence of impurities and additives, with a consequent enhancement of transport of oxidants, the tendency of the surface oxide product to crystallise and the evolution and release of CO. All of these factors markedly affect the oxidation rate.

In a first stage of oxidation at 1300°C ($t > 30$ h) a parabolic relationship closely fits the experimental weight gain data: the calculated oxidation rate constant

is 4.3×10^{-4} mg^2/(cm^4 min). If a parabolic model is assumed for the whole time of oxidation, the oxidation rate constants at 1000 and 1300°C are found to be 8.4×10^{-7} and 3.0×10^{-4} mg^2/(cm^4 min), respectively. The parabolic rate constant measured at 1300°C is two orders of magnitude higher than those found for the oxidation of pure CVD SiC,[8–21] but falls in a range of values reported for the oxidation of SiC sintered with various sintering aids.[9,16,17] It confirms that sintering aids invariably accelerate the oxidation rate compared with that measured for pure materials.[8,21] The reason for this is reduced viscosity of the glassy film in the
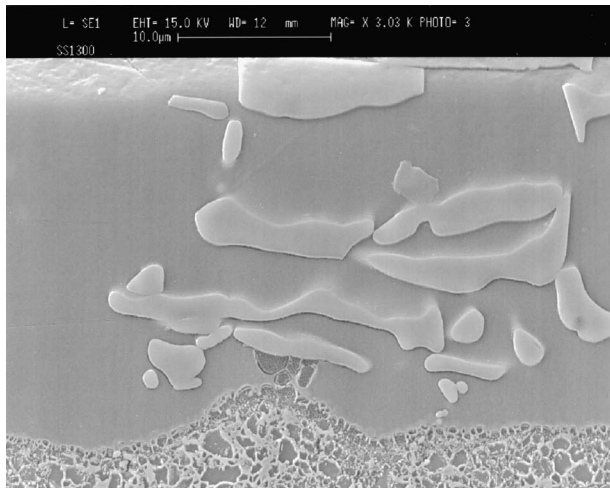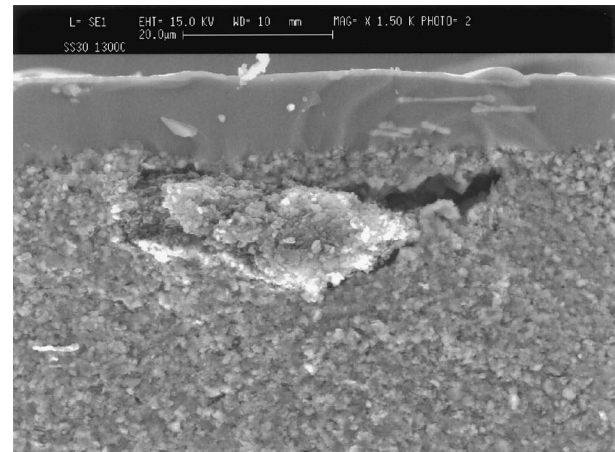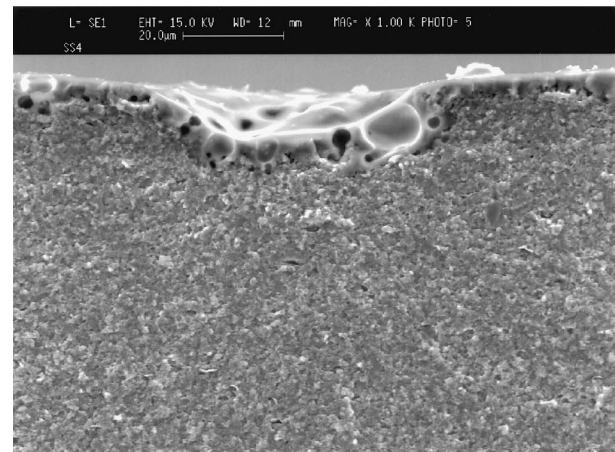

(a)
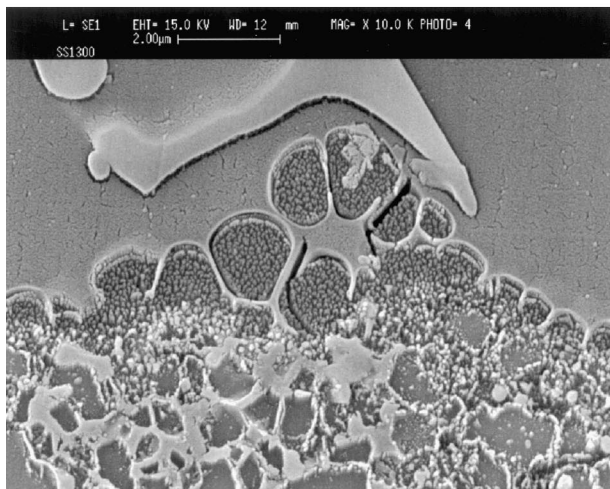
(b)

Fig. 13. SEM micrographs of plasma etched sections through ceramic and surface scale: (a) and (b) the sharp interfaces, decorated with crystobalite crystals, between surface oxide and base ceramic after oxidation for 50 h at 1300°C.

(a)

(b)

Fig. 14. SEM micrographs of fracture sections through the ceramic showing various defects: (a) an intrinsic flaw in the ceramic, immediately below the base of the surface scale; (b) an oxidation-induced pit causing fracture to be initiated at the surface.

Table 4
Flexural strength (σ) after 50 h of corrosion/oxidation of SiC and comparison with the as-sintered material

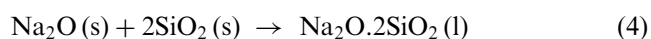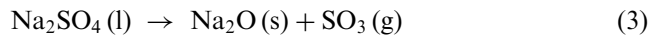|	As sintered	1000°C (1% S)	1000°C (0.01% S)	1300°C (1% S)	1300°C (0.01% S)	1000°C (laboratory air)	1300°C (laboratory air)
σ (MPa)	656±58	698±75	463±64	428±28	437±26	602±152	611±161

presence of sintering aids, the low viscosity permitting enhanced diffusion of oxygen. While insufficient data are available for an apparent activation energy to be determined, an estimate using rate data for the two test temperatures gives a value of 320 kJ/mol. This value agrees well with other published values[16–18] for similar materials. However the value of the apparent activation energy accounts for a rate controlling mechanism different from the diffusion of oxygen through the growing amorphous silica film (120–140 kJ/mol). While an alternative mechanism to account for the high activation energy has never been agreed, one hypothesis is that the crystallization of the oxide film could play a decisive role. Activation energies of 272 kJ/mol have been found for the oxidation of silicon when the film that formed was crystalline. Another hypothesis suggests that the desorption of CO(g) from the SiC/SiO$_2$ interface could be the rate controlling process,[17] but in the present work the evolution of CO (g) occurs mainly through a pore and bubble network in the oxide layer. It is more likely, therefore, that diffusion in the unoxidized material of the additive- and impurity-cations towards the reaction interface is the rate controlling process in the oxidation of liquid-phase sintered SiC. This has been suggested elsewhere[18] and is in agreement with other authors and is also substantiated by the analogy with the phenomena occurring in Si$_3$N$_4$-based materials.[14,22]

4.2. Burner rig corrosion

The total weight gains measured after 50 h at 1000°C, respectively for the tests with 1% and 0.01% sulphur fuels, were 4 and 12 times greater than that measured after oxidation in air. For burner rig tests at 1300°C the weight gain was around 3 times greater. Combustion environments clearly accelerate the rate of material degradation compared to that observed in air. The main element responsible for the difference is sodium, which is incorporated in the silicate glass (Fig. 4). The sources of Na in the combustion gas are numerous salts, mainly originating from NaCl in the ingested air. The species shown in Table 2 are in thermodynamic equilibrium in the combustion gases. The question regarding which, or whether one of these species is more important than the others, has not yet been established. A number of proposals have, however, been made to account for the observed degradation.

At temperatures up the dew point of Na$_2$SO$_4$, decomposition results in the formation of Na$_2$O. The basic nature of Na$_2$O results in reaction with SiO$_2$ which is acidic:[9]

$$Na_2SO_4\,(l) \;\rightarrow\; Na_2O\,(s) + SO_3\,(g) \qquad (3)$$

$$Na_2O\,(s) + 2SiO_2\,(s) \;\rightarrow\; Na_2O.2SiO_2\,(l) \qquad (4)$$

In a dynamic combustion environment, reaction (Eq. 3) is shifted to the right by reducing the production of SO$_3$. Hence, increased production of Na$_2$O, with the consequence that the formation of liquid Na$_2$Si$_2$O$_5$ [Reaction (4)], is promoted in combustion gases derived by burning low-sulphur fuels. Increasing the concentration of Na$_2$O leads to a progressive decrease of viscosity of the surface silicate. Low viscosity leads to increased rates of transport and subsequently to enhanced rates of attack of the ceramic. This scenario agrees with the experimental results obtained in burner rig tests carried out at 1000°C.

With the 0.01% S fuel an approximately linear rate of weight change up to 30 h was observed. This was followed by a decreased rate of change. After 50 h a surface scale up to 50 μm thick was accompanied by internal attack, in the form of extensive pitting, to a depth of 100 μm in the ceramic. Due to the enhanced rate of transport through the liquid sodium silicate, the chemical reaction at the interface would presumably be responsible for rate control during the linear stage of exposure. Subsequently, enhanced diffusion of additives and phenomena such as crystallisation in the reaction product and bubble formation, could have lowered the oxygen transport through the surface layers, resulting in nearly parabolic behaviour.

With the 1% S fuel, the behaviour was completely different. The rate of corrosion was low and the surface scale was very thin (2 μm). The comparatively high rate of weight gain in the initial, transient stage (up to 6.5 h) is attributed to the rapid formation of a continuous SiO$_2$-rich surface layer. The initial period is characterised by the rapid formation of SiO$_2$, which seals pores and covers grain boundary material at the surface of the ceramic. Subsequently, the rate of weight gain was very low due to the high partial pressure of SO$_3$ inhibiting the formation of Na$_2$O. A low Na$_2$O activity means that little Na is incorporated into the silicate glass, viscosity remains high and diffusion processes are slow.

At temperatures above the dew point of Na$_2$SO$_4$ (1000°C is just above the dew point of Na$_2$SO$_4$ for the conditions used in this work), the major Na-containing compound is NaOH (Table 2) which may react with SiO$_2$ directly:

$$2NaOH\,(g) + 2SiO_2\,(s) \;\rightarrow\; Na_2O.2SiO_2\,(l) + H_2O\,(g)$$

$$(5)$$
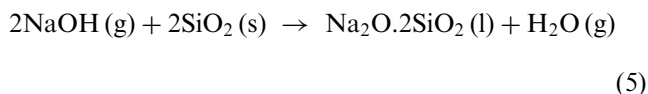
In principle, this reaction should be independent of the partial pressure of SO$_3$, and therefore the rate of surface attack should be equal for low- and high-sulphur fuel. Broadly similar modes of degradation were observed for the tests with 1 and 0.01% sulphur fuels at 1300°C. Under both conditions, an initial linear stage of weight gain was recorded. In the 0.01% S fuel the linear

stage extended to 30 h with the weight gain of around 2 mg cm^{-2}, while in the 1% S fuel a similar amount of weight was gained during a shorter linear stage (12 h). In both cases the linear rate suggests an interfacial reaction controlled mechanism during the initial stages of exposure. The end of the linear stage in the 0.01% S fuel coincided with gas bubble (mainly CO) bursting at the outer surface [Fig. 5(b)] and a sudden decrease in test piece weight. At this stage it was also noted that loss of oxidation products due to a combination of flow of the thick, low viscosity glassy material at the test temperature and due to spallation on cooling occurred rendering weight measurements unreliable for purposes of determining corrosion kinetics. Nevertheless, there was a rough correlation between overall thinning of the surface scale, scarcity of retained gas bubbles and small, steady increase in subsequent weight gain. Material loss was less evident on the test pieces exposed to the 1% S fuel combustion gas, where more gas bubbles were retained and the rate of weight change was lower. The wide scatter of the data did not allow a determination of whether the second stage was again linear or parabolic.

The amount of oxidation products formed at 1300°C was much greater than at 1000°C, and this is primarily due to the lower viscosity of the glass at the higher temperature. Similar oxidation product morphologies were produced in the respective combustion gases at 1300°C. In each case crystobalite was found at the scale-ceramic interface [Figs. 5(c) and 8(a)] and these crystals were covered by a Na-modified silicate glass. For similar Na-silicates to be formed in each case the Na activity must have been similar. Despite the large difference in SO3 partial pressure, the partial pressure of Na$_2$O is invariant at 1300°C, unlike at 1000°C (Table 2). Thus, whether the reaction of SiO$_2$ to the low viscosity silicate (Na$_2$O.2SiO$_2$) derives from Na$_2$O, or the more obvious source of Na, NaOH, reaction with the ceramic should be similar. The tendency for the crystobalite grains to form a more compact layer on the ceramic surface in the 0.01% S fuel gas [Fig. 5(c)] may be the reason for the lower rate of scale growth in the second growth regime. By comparison, the crystobalite grains were more easily detached from the ceramic surface upon exposure to the 1% S fuel gas [Fig. 9(a)]. Where a continuous crystobalite layer can be formed on the ceramic surface, this layer may constitute an effective diffusion barrier with the result that the subsequent rate of attack is reduced.

From a comparison of the air oxidation and burner rig test results, strong effects of the presence of contaminants from the combustion atmosphere on the kinetics of corrosion, on oxide scale composition and morphology and on the material damage below the reaction interface are clearly evident. In terms of flexural strength (Table 4), environmental attack can either strengthen or weaken the bulk material, depending upon the mode of corrosive attack. The room temperature flexural strength was found to increase after exposure to the 1% S fuel combustion gas at 1000°C, due in part to the corrosion process causing smoothing of the ceramic surface from that existing after machining. There was a negligible change in strength after exposure in air at 1000 and 1300°C. On the contrary, corrosion in the burner rig at both 1000 and 1300°C with the 0.01% S fuel resulted in large surface/sub-surface defects leading to substantial strength reduction. The defects were mainly in the form of discrete pits caused by localised attack of grain boundary material in the ceramic. The pits appeared to be associated with gas bubbles located at the scale-ceramic interface, as observed previously.[9] While oxidation should always result in the production of gas [reaction (1)], when bubbles become large and eventually burst, fresh SiC can be exposed to the combustion gas and the locally enhanced attack results in pitting [Figs. 7(a) and 14]. As a consequence of the locally enhanced attack more gas is produced and new gas bubbles form and so the whole process can become self-perpetuating.

5. Conclusions

From a study of the oxidation resistance of a liquid phase sintered SiC with Al$_2$O$_3$ and Y$_2$O$_3$ additives in laboratory air and in combustion gases, the following conclusions can be drawn:

1. The oxidation rate in air was found to approximate a parabolic law at temperatures of 1000 and 1300°C and an estimate of the apparent activation energy (320 kJ/mol) suggested the controlling mechanism not to be simply O$_2$ diffusion through SiO$_2$ as for pure SiC. The presence of the sintering additives increases the rate of oxidation of LPS-SiC by around 2 orders of magnitude compared with pure SiC.
2. Oxidation is the major reaction in combustion gases with the presence of contaminants, particularly Na, in the gas modifying both oxidation kinetics and oxidation product morphologies. The amount of attack is closely dependent upon the actual composition of the combustion gas, and thus on the fuel used; a low sulphur content fuel giving high rates of oxidation at 1000°C. The mechanism of the degradation process involves the formation of Na$_2$O, whose activity is determined by the SO$_3$ partial pressure, and the reaction with SiO$_2$ to produce a low viscosity silicate glass. At 1300°C, the rate of corrosion was found to be essentially independent of combustion fuel sulphur content.
3. The flexural strength of ceramics is closely influenced by the presence of surface defects. Oxidation

in air results in a negligible change in flexural strength, while the moderately more aggressive attack induced by a 1% S fuel combustion gas reduction can result in the size of pre-existing surface defects being reduced and strength increased. Following the more severe attack in a 0.01% S fuel combustion gas in which surface pits are created, flexural strength is significantly reduced.

Acknowledgements

References

1. Motzfeld, K., Silicon carbide: synthesis, structure and sintering. In *Proc. Int. Conf. Engineering Ceramics 92,* ed. M. Havier., Reprint, Bratislavia, 1993, pp. 7–42.
2. Dressler, W. and Riedel, R., Progress in silicon-based non-oxide structural ceramics. *Int. J. Refractory Metals and Hard Materials*, 1997, **15**, 13–47.
3. Kleebe, H. J., SiC and Si_3N_4 materials with improved fracture resistance. *J. Eur. Cer. Soc.*, 1992, **10**, 151–159.
4. Lange, F. F., Hot pressing behaviour of silicon carbide powders with additions of aluminium oxide. *J. Mater. Sci.*, 1975, **10**, 314–320.
5. van Dijen, F. K. and Mayer, E., Liquid phase sintering of SiC. *J. Eur. Ceram Soc.*, 1996, **16**, 413–420.
6. Falk, L. K., Microstructural development during liquid phase sintering of silicon carbide ceramics. *J. Eur. Ceram. Soc.*, 1997, **17**, 983–994.
7. Bellosi, A., Sciti, D., Melandri, C. and Dalle Fabbriche, D., Liquid-phase sintered silicon carbide: processing and properties. In: *Synthesis and Methodologies in Inorganic Chemistry—New Compounds and Materials*, Vol. 8, ed. S. Daolio et al. Litografica La Photograph, Padova, Italy, 1998, pp. 269–272.
8. Tressler, R. E., Theory and experiment in corrosion of advanced ceramics. In *Corrosion of Advanced Ceramics*, ed. K. G. Nickel. Kluwer Academic Publishers, The Netherlands, 1994, pp. 3–22.
9. Jacobson, N. S., Corrosion of silicon-based ceramics in combustion environment. *J. Am. Ceram. Soc.*, 1993, **76**(1), 3–28.
10. Luthra, K. L., Some new perspectives on oxidation of silicon carbide and silicon nitride. *J. Am. Ceram. Soc.*, 1991, **74**(5), 1095–1103.
11. Baxter, D. J., Burner rig hot salt corrosion of Si_3N_4 in the temperature range 800 to 1300°C. In *Corrosion of Advanced Ceramics*, ed. K. G. Nickel. Kluwer Academic Publishers, The Netherlands, 1994, pp. 249–259.
12. Costa Oliveira, F., Edwards, R. A. H. and Fordham, R. J., In *High Temperature Corrosion of Technical Ceramics,* ed. R. J. Forham. Elsevier Applied Science, 1990, pp. 53–67.
13. Graziani, T., Baxter, D. and Nannetti, C. A., Degradation of silicon carbide-based materials in high temperature combustion environment. In *Key Engineering Materials*, vol. 113, ed. R. J. BaxterD. J. Baxter and T. Graziani. Trans. Tech. Publications, Switzerland, 1996, pp. 153–164.
14. Bellosi, A., Oxidation behaviour of nitrides and borides as monolithic and composite ceramics. In *Corrosion of Advanced Ceramics*, ed. K. G. Nickel. Kluwer Academic Publishers, The Netherlands, 1994, pp. 131–142.
15. Sigl, L. S. and Kleebe, H. J., Core/rim structure of liquid phase sintered silicon carbide. *J. Am. Ceram Soc.*, 1993, **76**, 773–776.
16. Singhal, S. C. and Lange, F. F., Effect of alumina content on the oxidation of hot pressed silicon carbide. *J. Am. Ceram. Soc.*, 1975, **58**, 433–435.
17. Singhal, S. C., Oxidation Kinetics of hot pressed silicon carbide. *J. Mat. Sci.*, 1976, **11**, 1246–1253.
18. Costello, J. A. and Tressler, R. E., Oxidation Kinetics of hot pressed and sintered α-SiC. *J. Am. Ceram. Soc.*, 1981, **64**(6), 327–331.
19. Park, S. C., Cho, K. and Kim, J. J., Oxidation of hot pressed silicon carbide in the cyclic and static conditions. *J. Mat. Sci. Letters*, 1998, **17**, 23–25.
20. Eriksson, G., Thermodynamic studies of high temperature equilibria: SOLGASMIX, a computer program for calculation of equilibrium compositions in multi-phase systems. *Chemica Scripta*, 1975, **8**, 100–103.
21. Fox, D. S., Oxidation behavior of CVD silicon carbide and silicon nitride from 1200°C to 1600°C. *J. Am. Ceram. Soc.*, 1998, **81**(4), 945–959.
22. Cubicciotti, D. and Lau, K. H., Kinetics of oxidation of hot pressed Si_3N_4 containing magnesia. *J. Am. Ceram. Soc.*, 1978, **61**(11–12), 512–517.